Clays Clay Miner., Vol. 70, No. 4:492–513, 2022
https://doi.org/10.1007/s42860-022-00197-2

ORIGINAL PAPER

Characteristics and Formation Pathways of Iron- and Magnesium-Silicate-Hydrates and Smectites Under Natural Alkaline Conditions

Misato Shimbashi · Shingo Yokoyama · Ryosuke Kikuchi · Tsubasa Otake · Tsutomu Sato

Accepted: 3 August 2022 / Published online: 23 August 2022

Abstract Understanding the behavior of secondary minerals under alkaline conditions is important for predicting the potential alteration of the constituent minerals in radioactive-waste disposal facilities. A previous study reported the formation of uncommon Fe- and Mg-bearing clays under natural alkaline conditions in the Philippines; these were referred to as iron-magnesium-silicate-hydrates (F-M-S-H) and nontronite-like minerals. The current study aimed to investigate the structural and chemical characteristics and to understand the formation pathways of these clays by performing a detailed characterization. F-M-S-H comprised tetrahedral–octahedral–tetrahedral (TOT) layers, imperfect interlayer hydroxide sheets, and interlayer Ca ions. The systematic changes in the characteristics of F-M-S-H at different sampling depths, such as the gradual decrease of the interlayer hydroxide sheets to form smectitic domains, were caused by the differing interaction periods between each sediment at different sampling depths and alkaline seepage. Furthermore, F-M-S-H was ferrous in form prior to oxidation. In contrast, a nontronite-like mineral comprised nontronite and part of an interlayer hydroxide sheet. This mineral was inferred to be formed under chemically different conditions from F-M-S-H, and probably formed in the presence of aqueous Fe^{3+} and Mg ions.

Keywords Alkaline conditions · Interlayer hydroxide sheet · Iron-magnesium-silicate-hydrate · Nontronite · Radioactive-waste disposal

M. Shimbashi (✉) · S. Yokoyama
Geology and Geotechnical Engineering Division, Central Research Institute of Electric Power Industry, Abiko, Chiba 270-1194, Japan
e-mail: s-misato@criepi.denken.or.jp

M. Shimbashi
Division of Sustainable Resources Engineering, Graduate School of Engineering, Hokkaido University, Sapporo, Hokkaido 060-8628, Japan

R. Kikuchi · T. Otake · T. Sato
Division of Sustainable Resources Engineering, Faculty of Engineering, Hokkaido University, Sapporo, Hokkaido 060-8628, Japan

Introduction

Radioactive-waste disposal facilities use many types of materials as engineered barriers to isolate the radioactive waste, including cementitious materials, carbon steels, and bentonite (Sellin & Leupin, 2014). Alkaline conditions can be produced at radioactive-waste disposal facilities by the alteration of cementitious materials and iron corrosion. For example, cementitious materials, such as ordinary Portland cement (OPC) or low-pH cement, produce alkaline porewaters with a pH range of 10–13 (García Calvo et al., 2010), whereas a mixture of iron powder and water produces a solution with an approximate pH of 11 (Kaufhold et al., 2020). Although the Fe or Mg content in these alkaline radioactive waste disposal systems is not large, the potential formation of Fe- or Mg-bearing clays is discussed actively. Specifically, several types of Fe- or Mg-bearing clays are

known to be formed by the interaction between cementitious materials and bentonite (e.g. Fernández et al., 2018; Yokoyama et al., 2021), cementitious materials and clay rocks (e.g. Dauzeres et al., 2016; Lerouge et al., 2017), and iron and bentonite (e.g. Wilson et al., 2006). As the period for the safety assessment of the radioactive-waste disposal is rather extensive, natural analogue (NA) studies, in addition to the laboratory and in situ experiments described above, remain beneficial. The study of NA involves the observation of systems in nature which form analogues with the phenomena concerned with the disposal of radioactive waste. To increase the limited number of studies investigating NA, it has been suggested that the discipline should be pursued vigorously, taking a stance which allows for system analogues to be localized (Yoshida et al., 2010). In this context, understanding the formation reaction of secondary Fe- or Mg-bearing clays during natural, long-term alkaline interactions occurring in various geological settings would be useful, even if they were not the alteration of the constituent materials in radioactive waste disposal, to predict potential secondary minerals formed by the long-term alteration in radioactive-waste disposal.

Near the Troodos ophiolite in Cyprus, Fe-bearing palygorskite was formed by interaction between bentonite and alkaline water over a time span of 10^5–10^6 y (Milodowski et al., 2016). Similarly, the interaction between bentonite and alkaline water at the Saile mine in the Philippines produced Fe- and Mg-bearing smectites (Fujii et al., 2014). In the Denizli Province of Turkey, Akbulut and Kadir (2003) reported the formation of Fe-bearing palygorskite, sepiolite, and saponite in alkaline waters. Furthermore, Furquim et al. (2010) discovered Fe-illite and glauconite with amorphous phases in saline lakes in the Pantanal wetland of Brazil. Chrysotile and poorly crystalline chrysotile-like phases were reported as precipitates from alkaline water at near-surface or surface environments in New Zealand (Craw et al., 1987) and Japan (Nishiki et al., 2020).

In addition to these previous studies, the widespread distribution of uncommon Fe- and Mg-bearing clays under alkaline conditions at Narra in Palawan, the Philippines, were recently reported (Shimbashi et al., 2020). Although these clays have been reported to be authigenic and formed under alkaline conditions, their nature remains uncertain (Shimbashi et al., 2020) as shown in the next section below. The current study aimed to establish the structural and chemical characteristics and to understand the formation pathways of Fe- and Mg-bearing clays in alkaline fluids in the Narra District of the Philippines to add to existing knowledge regarding the naturally occurring Fe- and Mg-bearing clays under alkaline conditions.

Site Description and Previous Studies at The Site

The geological setting of the Narra District of the Philippines is dominated by the Palawan ophiolite, which comprises the Beaufort Ultramafic Complex, Stavely Gabbro, and Espina Formation (Aurelio et al., 2014). Because the generation of alkaline water has been reported frequently in the ultramafic rocks (Barnes et al., 1978), this study site was selected in order to understand geochemical reactions under natural alkaline conditions.

The sampling site comprises an alluvial fan channel on a gentle slope of the Palawan ophiolite basement (Fig. 1a). Eight trenches (T1–T8) and four drill holes (DH1–DH4) were excavated at depths below the surface ranging from 0 to 16 m (Fig. 1b). Clastic sediments, which overlaid the basement (Fig. 1a), were derived from serpentinized rocks and gabbro from the Palawan ophiolite (Shimbashi et al., 2020). The deposition of the sediments was determined to have been initiated 15,000 y ago based on ^{14}C dating of humin in the sediments (Table 1; Shimbashi et al., 2020), and the depositional environment of the sediments probably changed from seawater to brackish water and further to freshwater over time (RWMC, 2017; Shimbashi et al., 2020). The sediments interacted with alkaline (pH 11) seepage, which was produced by the geochemical reactions of meteoric water with the Palawan ophiolite (RWMC, 2016, 2017, 2018; Shimbashi et al., 2018). After deposition, a carbonate layer was formed on the surface through the mixing of alkaline water and surface water (Shimbashi et al., 2018).

The clastic sediments in this area comprised predominantly a mineral with a broad X-ray diffraction (XRD) peak at 14 Å (14 Å phase), orthopyroxene, amphibole, serpentine, talc, chlorite, calcite, and 14 Å tobermorite (Shimbashi et al., 2020). Newly formed phases in the sediments included Fe- and Mg-bearing clays (i.e. 14 Å phases) and 14 Å tobermorite. The Fe- and Mg-bearing clays were categorized previously into three types based on XRD analysis (Shimbashi et al., 2020). Type-I exhibited trioctahedral characteristics based on the d_{060} position, and its expandability after ethylene glycol (EG) treatment and its dehydration behavior (Fig. 2a) differed from those of smectite and chlorite. Type-II exhibited a

https://doi.org/10.1007/s42860-022-00197-2 Published online by Cambridge University Press

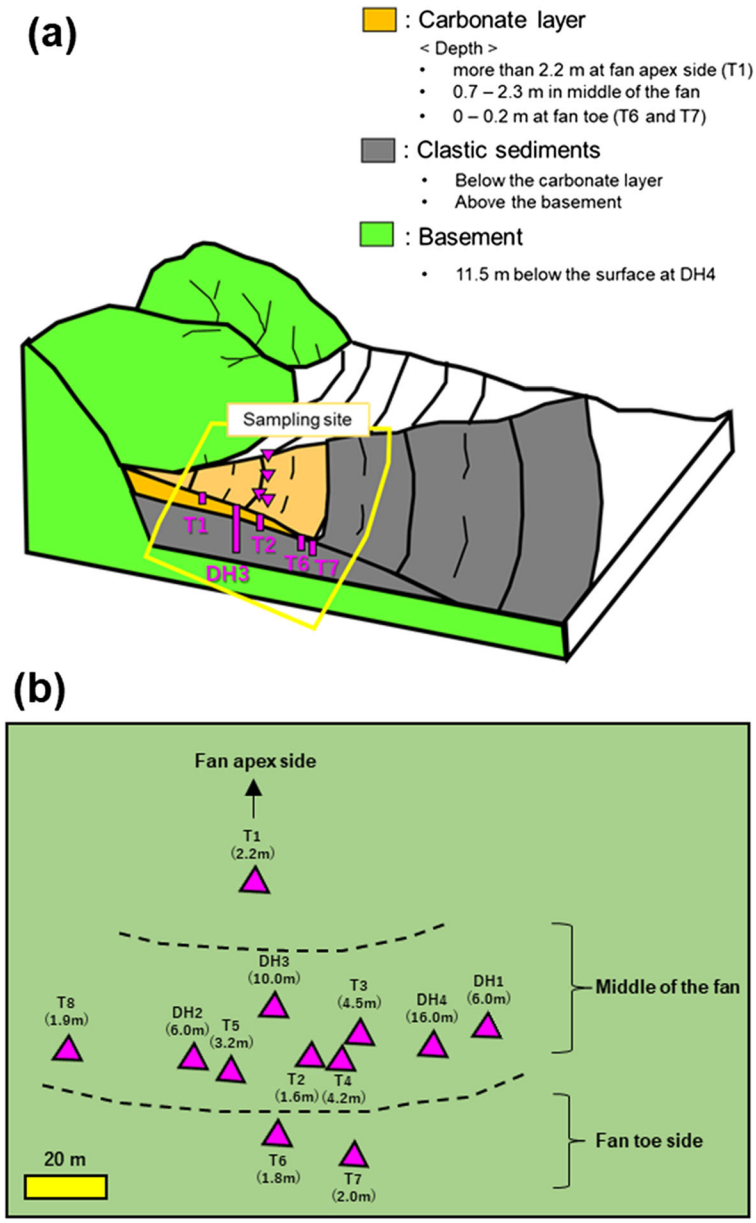

Fig. 1. **a** Conceptual diagram of the sample site (modified from Shimbashi et al. (2020)); and **b** aerial map showing the location of trenches and drill holes: the numbers in parentheses represent the total depths of the trenches and drill holes from the surface

nature intermediate to that of Type-I and trioctahedral smectite, according to the expandability after EG treatment and dehydration behavior (Fig. 2b and c). In contrast, Type-III displayed dioctahedral characteristics based on the d_{060} position and exhibited expandability after EG treatment similar to smectite, although the dehydration state implied the presence of other phases of smectite (Fig. 3). The uncertainty of the characterization above led to labeling both Types-I and II as iron-magnesium-silicate-hydrates (F-M-S-H), and Type-III as a nontronite-like mineral (Shimbashi et al., 2020).

The F-M-S-H and 14 Å tobermorite were recognized at shallower sampling depths in the middle of the fan, in the sediments deposited in freshwater (Shimbashi et al., 2020). The nontronite-like mineral was observed at a deeper sampling depth in the middle of the fan and at a shallower sampling depth at the fan toe side (Fig. 1b), in the sediments deposited in seawater. The correlation

https://doi.org/10.1007/s42860-022-00197-2 Published online by Cambridge University Press

Table 1 Sample descriptions and *d* values obtained from the XRD analyses

Sample name	Trench or drill hole number	Depth (m)	^{14}C age (^{14}C y BP)	d_{001} after EG treatment (Å)	d_{001} during heating at 250°C (Å)	Major d_{060} (Å)	Type	Terminology
T2-7	T2	0.8	1900 *	16.0	–	1.53	–	F-M-S-H
T2-2		1.4	2560 *	15.4	–	1.54	–	F-M-S-H
T3-4	T3	2.7	6270 *	16.2	–	1.54	–	F-M-S-H
T3-2		3.1	7210 *	16.5	–	1.54	–	F-M-S-H
T4-3	T4	2.8	5060 *	16.4 *	13.6 + 10.1 *	1.53 *	Type-II *	F-M-S-H
T4-1		3.9	6300 *	16.7 *	14.7 + 10.0 *	1.52 + 1.54 *	Type-II + Type-III *	–
T7-7	T7	0.7	4010 *	17.0 *	14.6 + 10.1 *	1.51 *	Type-III *	Nontronite-like mineral
T7-4		1.5	4590 *	17.0	–	1.51	–	Nontronite-like mineral
DH1-7	DH1	2.2	4520 *	15.9 *	14.6 *	1.53 *	Type-I *	F-M-S-H
DH1-4		3.7	9010 *	16.7 *	15.3 + 9.9 *	1.54 *	Type-II *	F-M-S-H
DH3-14	DH3	1.9	–	15.7	–	1.54	–	F-M-S-H
DH3-12		3.5	6450 *	16.5	–	1.54	–	F-M-S-H
DH3-9		6.1	–	16.9	–	1.52 + 1.54	–	–
DH3-6		7.3	11480 *	17.0	–	1.51	–	Nontronite-like mineral
DH3-3		8.3	–	17.0	–	1.51	–	Nontronite-like mineral
DH3-1		10.0	15000 *	17.0 *	14.9 + 9.9 *	1.51 *	Type-III *	Nontronite-like mineral
DH4-12	DH4	3.2	6070 *	16.2	–	1.54	–	F-M-S-H
DH4-9		8.0	14110 *	17.0 *	15.1 + 9.9 *	1.51 *	Type-III *	Nontronite-like mineral

*indicates data sourced from Shimbashi et al. (2020). Values for carbon isotope measurements were obtained from humin in the sediments.

between the distribution of secondary minerals and the depositional environment suggested that the depositional environment determined the species of secondary minerals. Specifically, the F-M-S-H and 14 Å tobermorite were considered to have been formed through the interaction between clastic sediments and alkaline seepage without seawater infiltration, whereas the nontronite-like mineral was formed presumably by a similar interaction with the involvement of seawater (Shimbashi et al., 2020).

Materials and Methods

Samples, which were numbered successively from bottom to top, were selected to represent the sediment from all the trenches and drill holes except for the T8, DH2, and T7-2 samples. This is because the spatial distribution of primary and secondary minerals, as well as depositional age and depositional environment in those sediment samples, had already been examined thoroughly in a previous study (Shimbashi et al., 2020). In the present study, a <2 μm fraction from the 18 samples, including the seven samples analyzed by Shimbashi et al. (2020), were selected and examined to understand the structural and chemical characteristics of the Fe- and Mg-bearing clays. To obtain the <2 μm solid fraction, the sediment samples were dispersed in distilled water and centrifuged for 4 min at 1000 rpm (190×*g*) using an ST-720M rotor and centrifuge (Kubota 4000 centrifuge, Tokyo, Japan) to form a <2 μm supernatant. The supernatant was further centrifuged for 10 min at 14,000 rpm (27,172×*g*) using an NA-8 rotor and centrifuge (TOMY Suprema21, Tokyo, Japan). The <2 μm solid fraction obtained was dried in a vacuum.

Following the drying of the solid fraction, an XRD analysis of the 18 oriented samples was conducted using

https://doi.org/10.1007/s42860-022-00197-2 Published online by Cambridge University Press

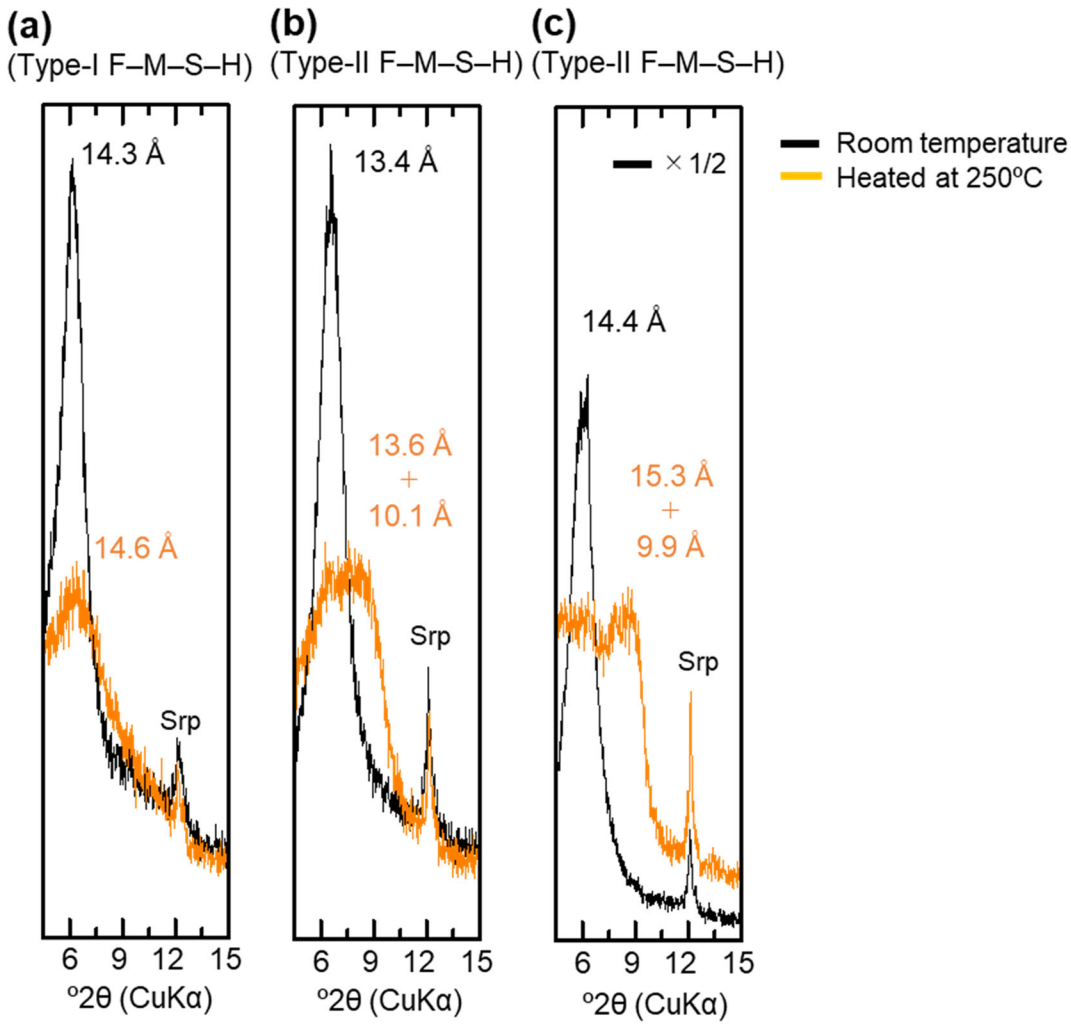

Fig. 2. XRD profiles of F-M-S-H before and during heat treatment at 250°C; **a** DH1-7; **b** T4-3; **c** DH1-4; data sourced from Shimbashi et al. (2020)

an X-ray diffractometer (Rigaku Smart Lab, Tokyo, Japan) with CuKα radiation set to 45 kV and 30 mA, at a scanning speed of 5°2θ/min, and a scanning step size of 0.01°2θ. The following slits were applied: divergence slit of 1/12°2θ, receiving slit of 20 mm, and a solar slit of 2.5°2θ. For the preparation of the oriented sample, 10 mg of the <2 μm samples was resuspended in distilled water and transferred onto a glass slide for the XRD analysis. After analysis, the oriented samples were further solvated with EG vapor at 60°C for >12 h, after which the XRD analysis was conducted on the EG-solvated samples using the same method as for the oriented samples. The randomly oriented samples of the <2 μm fraction were measured using XRD to observe the d_{060} of the Fe- and Mg-bearing clays. The XRD analyses for the randomly oriented samples were similarly conducted with CuKα radiation set to 45 kV and 30 mA, at a scanning speed of 0.3°2θ/min, and a scanning step size of 0.01°2θ. The following slits were also applied: divergence slit of 1/12°2θ, receiving slit of 20 mm, and a solar slit of 2.5°2θ.

A chemical analysis was conducted for 10 samples selected from the XRD results to represent the diversity of the samples. The Fe- and Mg-bearing clays were analyzed chemically using field emission scanning electron microscopy (FESEM) with energy dispersive X-ray spectroscopy (FESEM-EDS; JEOL JSM-7001M, Tokyo, Japan). The chemical composition of ~50 points was analyzed for each sample, and the median values of elemental ratios in each sample were compared.

https://doi.org/10.1007/s42860-022-00197-2 Published online by Cambridge University Press

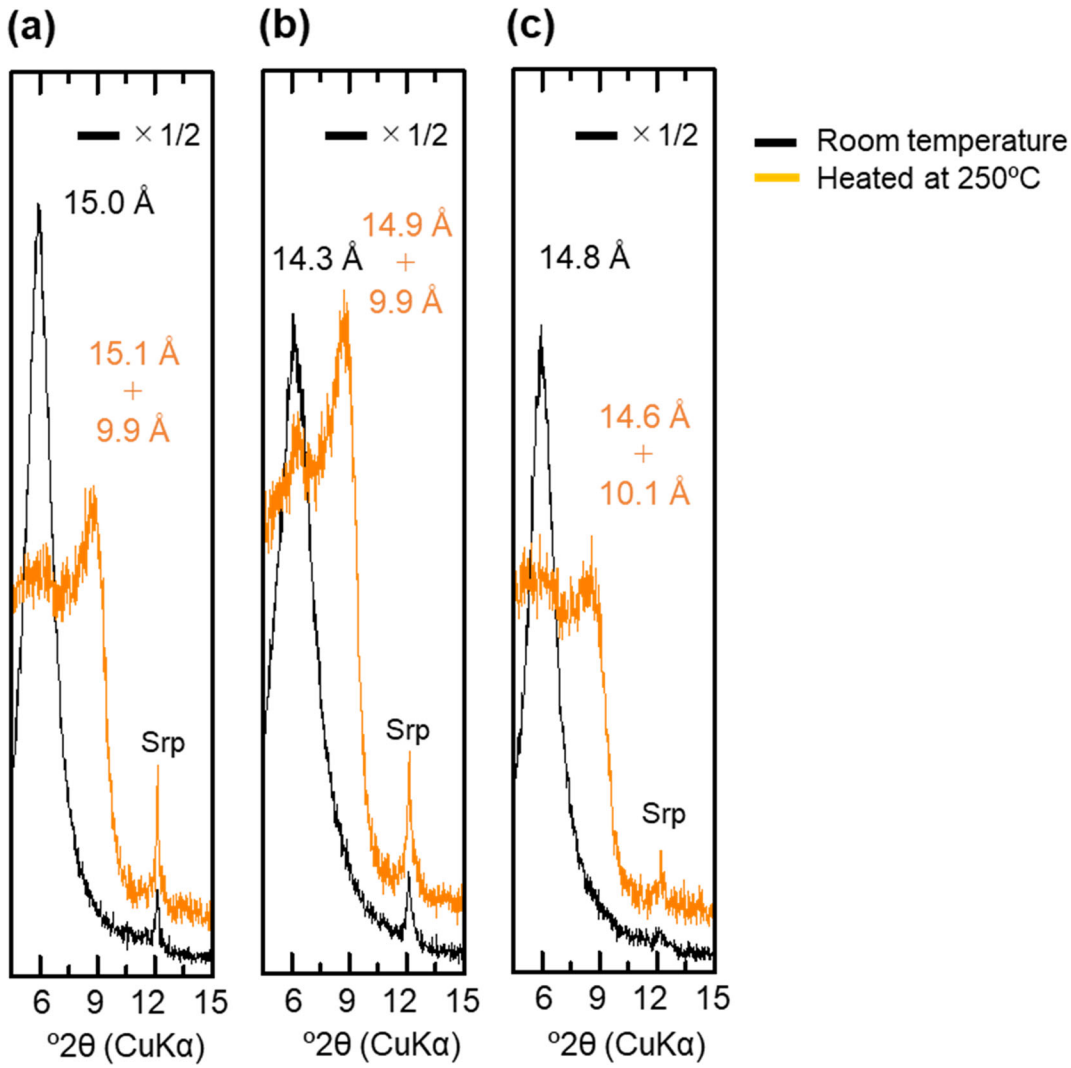

Fig. 3. XRD profiles of nontronite-like mineral before and during heat treatment at 250°C; **a** DH4-9; **b** DH3-1; **c** T7-7; data sourced from Shimbashi et al. (2020)

^{57}Fe Mössbauer spectroscopy was conducted at room temperature and 77 K using ^{57}Co in metallic Rh as a gamma-ray source. The <2 μm fractions in the DH1-7, DH1-4, and DH4-9 samples were selected as representative samples of F-M-S-H at shallower sampling depths, F-M-S-H at moderate sampling depths, and nontronite-like mineral, respectively (Table 1). The velocity scale was calibrated using a spectrum of α-Fe measured at room temperature as well as at 77 K. The spectra were fitted to a sum of doublets using a least-squares computer program and were characterized by three doublets. Isomer shifts (IS) are sensitive to the oxidation state and the coordination number of Fe ions and were allotted regarding α-Fe. Quadrupole splitting (QS) is a measure of the electric field gradient at the ^{57}Fe nucleus.

The infrared (IR) spectra were obtained using the three samples subjected to Mössbauer spectroscopy. The <2 μm samples were examined as KBr pellets which were dried for 1 day at 110°C and cooled in a desiccator filled with silica gel before analysis. The spectra were recorded from 100 scans at a resolution of 4 cm^{-1}, between 3800 to 370 cm^{-1}, using a Ge/KBr beam-splitter and a DLATGS detector on a Fourier-transform infrared spectrometer (JASCO FT/IR-6100, Tokyo, Japan).

The additional detailed analyses described below were conducted for F-M-S-H in the DH1-7 samples.

https://doi.org/10.1007/s42860-022-00197-2 Published online by Cambridge University Press

This was because F-M-S-H in the DH1-7 samples (Type-I) exhibited a behavior in the XRD analysis during heating at 250°C that was different from Type-II F-M-S-H and the Type-III nontronite-like mineral (Figs 2 and 3; Shimbashi et al., 2020). For the purpose of dissolving the interlayer hydroxide sheets between tetrahedral-octahedral-tetrahedral (TOT) layers (Rich & Bonnet, 1975), an acid treatment was performed for the <2 μm fractions of the DH1-7 samples. Although the acid treatment conditions differed from those used in a previous study (Rich & Bonnet, 1975), it was conducted at room temperature (~23°C) by adding 50 mg of the <2 μm fraction to 5 mL of a 0.1 M HCl solution and shaking for 30 min. To understand species of interlayer cations, an alkylammonium treatment was conducted by adding 15 mg of the <2 μm fraction to 5 mL of a 0.1 M dodecylamine hydrochloride (nC = 12) solution and incubating at 65°C for 2 days. The suspension for the alkylammonium treatment was separated using centrifugation, and the solid sample was redispersed in 5 mL of a 0.1 M dodecylamine hydrochloride solution and incubated at 65°C for 3 days. The acid-treated or alkylammonium-treated <2 μm fractions were washed with 80 or 100% ethanol several times until the supernatants were chloride free. The oriented sample was prepared using the washed samples. The acid-treated sample was solvated with EG vapor at 60°C for over 12 h, whereas the alkylammonium-treated sample was dried at 65°C for over 1 h before analysis. The XRD analysis of those samples was conducted using the same method as that used for the oriented samples.

The acid-treated <2 μm fraction was also examined by the XRD analysis with heat treatment. Because the sample amount was limited, the heat treatment was performed differently from that of a previous study, which analyzed the <2 μm fraction without acid treatment (Shimbashi et al., 2020). Specifically, 10 mg of the acid-treated <2 μm fraction was resuspended in distilled water, transferred onto a silica glass slide, and dried. The acid-treated sample was analyzed using XRD, like the oriented samples described above. After the XRD analysis, the acid-treated sample was heated at 250°C for 2 h in a muffle furnace, and the sample was cooled in a desiccator filled with silica gel. The XRD analysis of the heated sample was conducted similarly to the oriented samples within 10 min of heating.

The chemical components of the acid-treated or alkylammonium-treated <2 μm fractions were obtained using FESEM-EDS in the same manner as described above. The variation in chemical composition before and after the acid or alkylammonium treatments were displayed using box-and-whisker plots.

Results

XRD Analysis

The <2 μm fractions were composed predominantly of 14 Å phases with trace amounts of serpentine (Fig. 4a, c, and e). The d_{001} of the 14 Å phases shifted to a lower angle following EG treatment; it could not be determined, however, if the XRD reflection linked to the 001 reflection followed rationality in some samples, due to a small peak intensity (Fig. 4a). All of the 14 Å phases, except for samples T4-1 and DH3-9, were divided into F-M-S-H and nontronite-like mineral categories (Table 1 and Fig. 4), based on the values for d_{001} after EG treatment and d_{060} of the 14 Å phases (Shimbashi et al., 2020). Sample T4-1 represented a mixture of F-M-S-H and nontronite-like mineral (Shimbashi et al., 2020), probably the same for DH3-9. The distribution of F-M-S-H and nontronite-like mineral was identical to the trend reported in a previous study (Shimbashi et al., 2020), despite the increased number of samples analyzed in the current study. Moreover, the d_{001} after EG treatment of the F-M-S-H phases increased with increasing sampling depth, whereas that of all nontronite-like minerals showed the same expandability despite differences in the sampling depth (Fig. 5).

Chemical Composition

The chemical composition of both F-M-S-H and the nontronite-like mineral consisted mostly of Fe, Mg, Si, Ca, and Al ions. In the ternary diagram of Al-Mg-Fe, F-M-S-H plotted in a similar position to that of the nontronite-like mineral (Fig. 6a). Both the F-M-S-H and nontronite-like mineral were rich in Fe and Mg, and poor in Al. However, clear differences in the chemical composition between F-M-S-H and the nontronite-like mineral were recognized in the ternary diagram of Ca–Si–Fe+Mg+Al (Fig. 6b). F-M-S-H exhibited a chemical composition slightly richer in Ca and slightly poorer in Si than that of saponite, the trioctahedral smectite. The nontronite-like mineral was similar, in terms of chemical composition, to the ideal nontronite, the dioctahedral smectite.

https://doi.org/10.1007/s42860-022-00197-2 Published online by Cambridge University Press

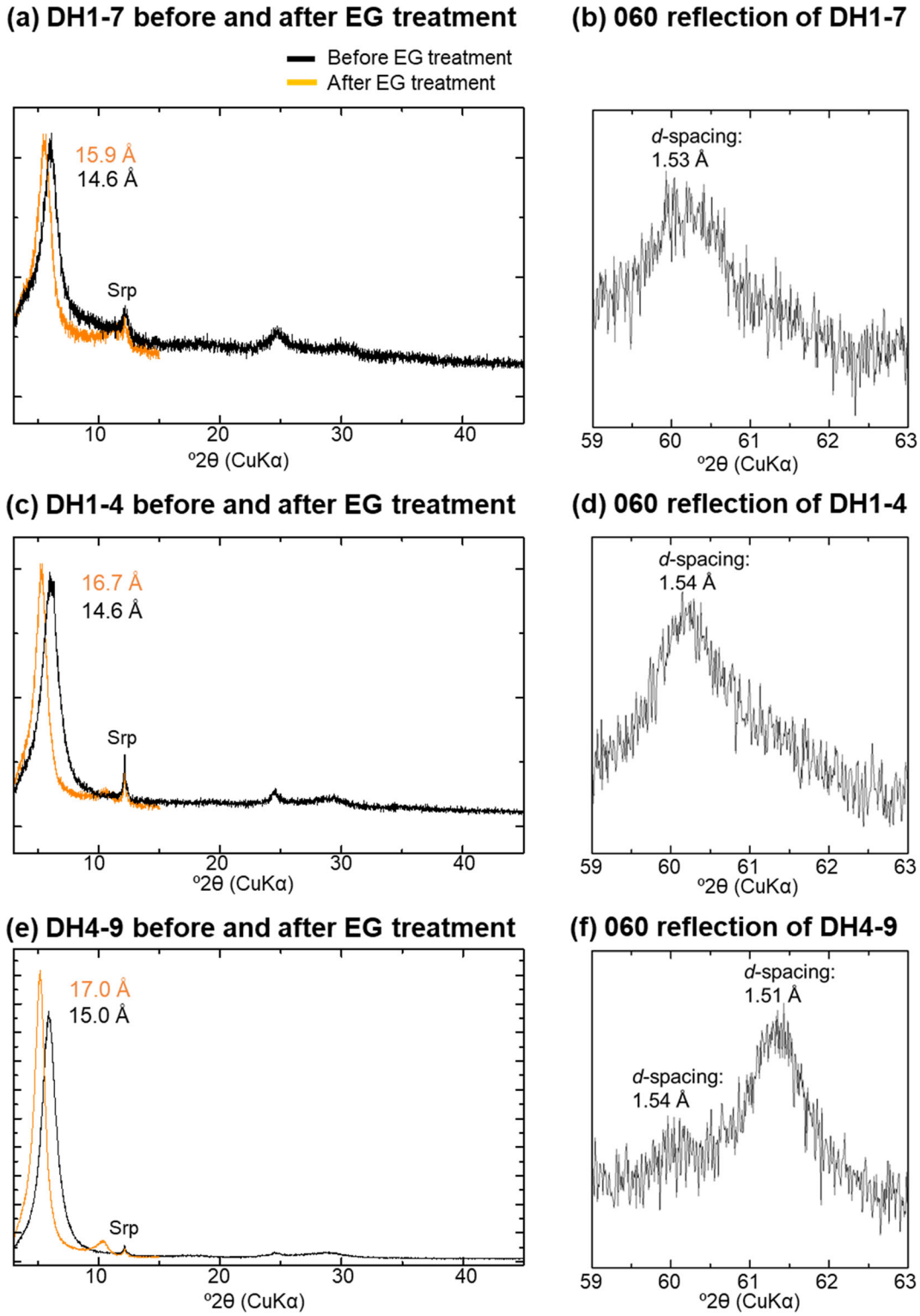

Fig. 4. XRD profiles before and after EG treatments of oriented samples and 060 reflection of randomly oriented samples; **a** and **b**: DH1-7; **c** and **d**: DH1-4; **e** and **f**: DH4-9; Srp: serpentine; data sourced from Shimbashi et al. (2020)

https://doi.org/10.1007/s42860-022-00197-2 Published online by Cambridge University Press

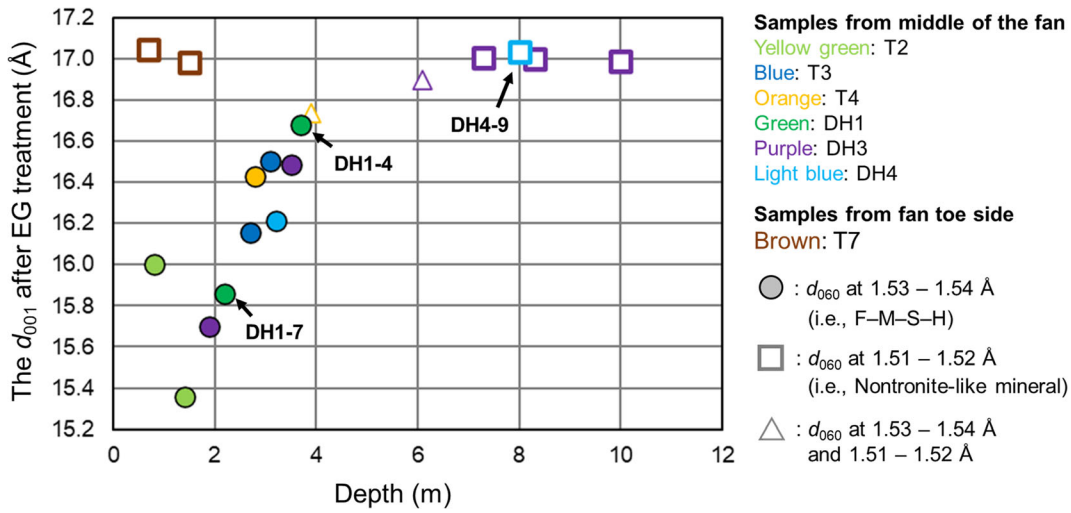

Fig. 5. d_{060} and d_{001} after EG treatment at different sampling depths

The median values of the (Fe+Mg)/(Si+Al) ratio, the (Fe+Mg+Al)/Si ratio, the Fe/Mg ratio, and the Al/(Si+Al) ratio of the F-M-S-H decreased continuously with increasing sampling depth, whereas the ratios of all nontronite-like minerals displayed relatively similar values (Fig. 7a–d). Furthermore, the median value of the Ca/(Si+Al) ratio of the F-M-S-H ranged between 0.08 and 0.15, while that of the nontronite-like mineral exhibited lower values ranging between 0.02 and 0.06 (Fig. 7e and Table 2).

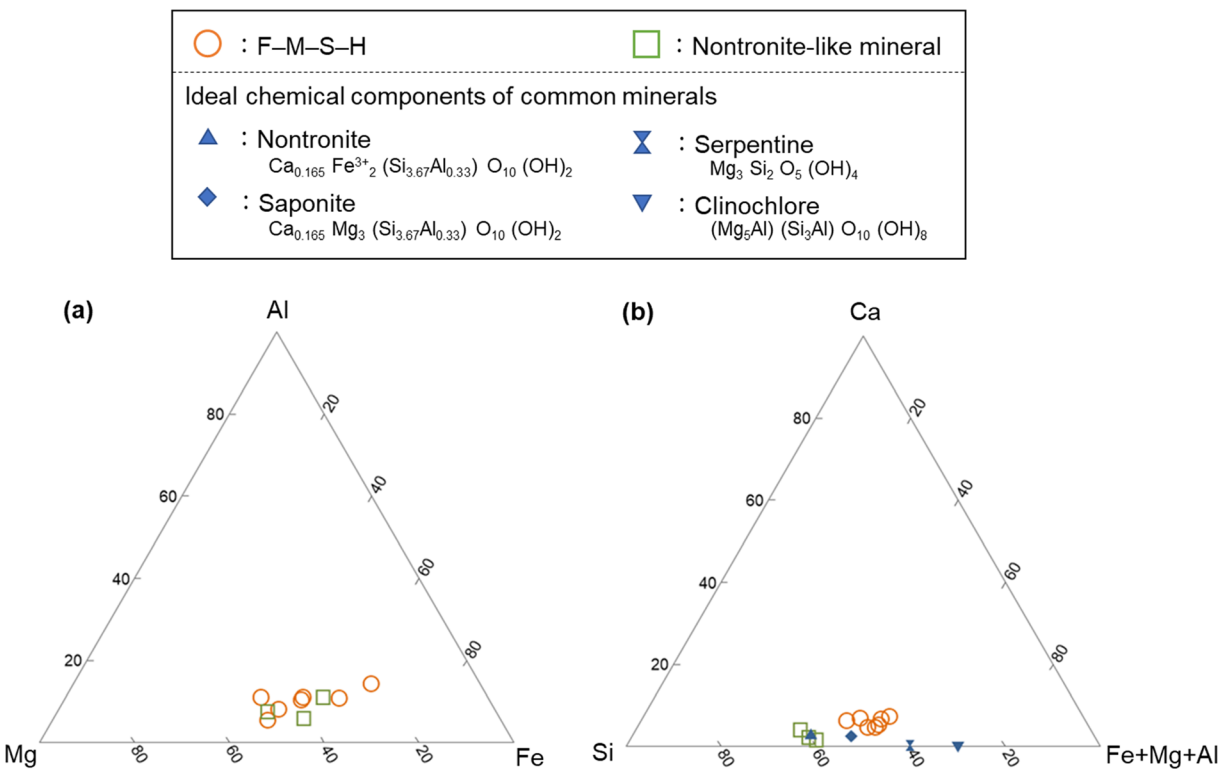

Fig. 6. Chemical compositions in ternary diagram: **a** ternary diagram of Al–Mg–Fe; **b** ternary diagram of Ca–Si–Fe+Mg+Al

https://doi.org/10.1007/s42860-022-00197-2 Published online by Cambridge University Press

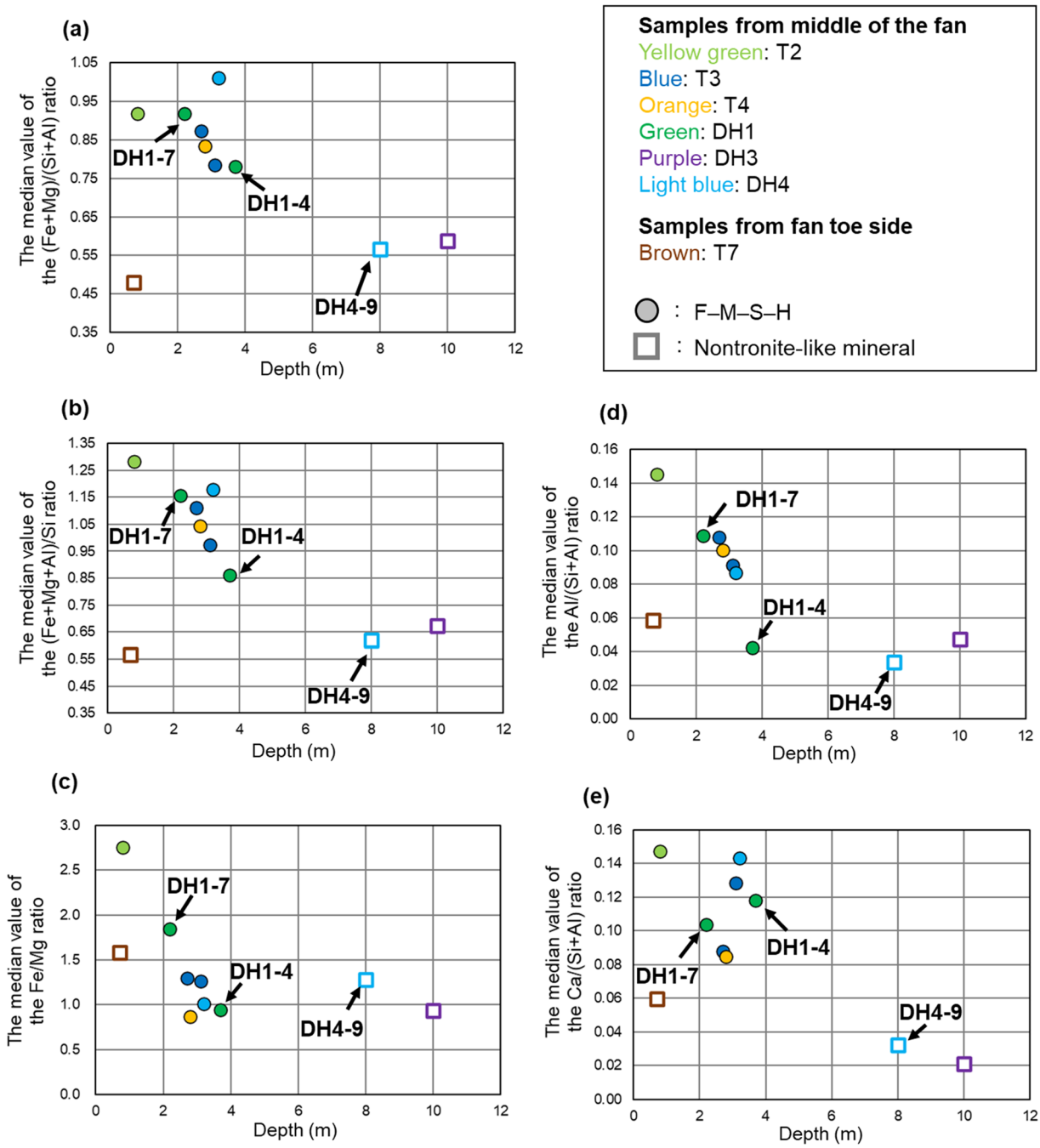

Fig. 7. Chemical compositions at different sampling depths: **a** (Fe+Mg)/(Si+Al) ratios; **b** (Fe+Mg+Al)/Si ratios; **c** Fe/Mg ratios; **d** Al/(Si+Al) ratios; **e** Ca/(Si+Al) ratios

Mössbauer Spectroscopy Analysis

The Mössbauer spectra of the F-M-S-H were similar, regardless of sampling depth (Fig. 8a, b, d, and e). They displayed two dominant Fe^{3+} doublets (Tables 3 and 4). The IS and QS values of the Fe^{3+} inner-doublet at room temperature (Table 3) exhibited similar values to that of Fe^{3+} in the octahedral site of the TOT layer for nontronite, which recorded an IS and a QS of 0.38 and 0.63 mms^{-1} at room temperature, respectively (Johnston

https://doi.org/10.1007/s42860-022-00197-2 Published online by Cambridge University Press

Table 2 The median values of chemical composition ratios

Sample name	Depth (m)	(Fe+Mg)/(Si+Al) ratios	(Fe+Mg+Al)/Si ratios	Fe/Mg ratios	Al/(Si+Al) ratios	Ca/(Si+Al) ratios
T2-7	0.8	0.92	1.28	2.75	0.15	0.15
T3-4	2.7	0.87	1.11	1.29	0.11	0.09
T3-2	3.1	0.78	0.97	1.27	0.09	0.13
T4-3	2.8	0.83	1.04	0.86	0.10	0.08
T7-7	0.7	0.48	0.57	1.58	0.06	0.06
DH1-7	2.2	0.92	1.15	1.85	0.11	0.10
DH1-4	3.7	0.78	0.86	0.94	0.04	0.12
DH3-1	10.0	0.59	0.67	0.93	0.05	0.02
DH4-12	3.2	1.01	1.18	1.01	0.09	0.14
DH4-9	8.0	0.57	0.62	1.28	0.03	0.03

& Cardile, 1985). Additionally, similar values of Fe^{3+} were shown in the octahedral interlayer hydroxide sheet of chlorite and recorded an IS and a QS of 0.34 and 0.69 mms^{-1} at room temperature, respectively (Czaja et al., 2014). On the other hand, the Fe^{3+} outer-doublet was characterized by high QS values (Tables 3 and 4). The IS and QS values of the Fe^{3+} outer-doublet (Tables 3 and 4) showed similar values of iron in octahedral sheets in the oxidized chlorite, which recorded an IS of 0.36 mms^{-1} and a QS of 1.04 mms^{-1} at 300 K, respectively, as well as an IS of 0.41 mms^{-1} and a QS of 0.94 mms^{-1} at 4 K (Kodama et al., 1982). Furthermore, similar values were found in the oxidized trioctahedral smectite which was previously ferrous iron-bearing (e.g. ferrian saponite), with an IS and a QS of 0.36–0.38 mms^{-1} and 1.31–1.38 mms^{-1} at room temperature, respectively (Treiman et al., 2014). In addition to the Fe^{3+} doublets, a minor Fe^{2+} doublet was also recognized, but the area ratio of the doublet was <8% (Tables 3 and 4).

The Mössbauer spectra of the nontronite-like mineral differed from that of F-M-S-H and exhibited a predominant Fe^{3+} inner-doublet (Fig. 8 and Tables 3 and 4). The IS and QS values of the Fe^{3+} inner-doublet at room temperature (Table 3) displayed similar values to that of Fe^{3+} in the octahedral site of the TOT layer of nontronite, which exhibited an IS of 0.38 mms^{-1} and a QS of 0.25 mms^{-1} at room temperature (Johnston & Cardile, 1985). In addition, minor Fe^{3+} outer-doublets were also recognized. The IS and QS values for the outer-doublet at room temperature (Table 3) was similar to that of Fe^{3+} in the octahedral site of the TOT layer of chlorite, which had an IS of 0.41 mms^{-1} and a QS of 1.03 mms^{-1} (Zazzi et al., 2006). The outer-doublet also exhibited similar values to the interlayer Fe^{3+} ions of nontronite, which recorded an IS of 0.48 mms^{-1} and a QS of 1.94 mms^{-1} at room temperature (Johnston & Cardile, 1985). An Fe^{2+} doublet was barely detected, and the area ratio of the doublet was <2% (Tables 3 and 4).

FTIR Spectra

The FTIR spectra for the OH-stretching vibration zones of both F-M-S-H and the nontronite-like mineral exhibited bands at 3676–3684 cm^{-1} (Fig. 9a), and were attributed to Mg_3–OH stretching vibrations in the octahedral sheet (Grauby et al., 1994; Madejová, 2003). The bands at 3538–3547 cm^{-1} may have arisen from Fe_2^{3+}–OH vibrations (Grauby et al., 1994; Zviagina et al., 2004). Because the bands at 3538–3547 cm^{-1} were broad, the bands from Fe^{3+}–OH–Mg vibrations at 3630 cm^{-1} can be added to these broad bands (Grauby et al., 1994). The bands at 3412–3414 cm^{-1} were due to adsorbed water (Brindley et al., 1979). Indeed, bands corresponding to water adsorbed by smectites were also observed previously even after heating pellets before the analysis (Zviagina et al., 2004).

The FTIR spectra of all samples exhibited strong bands at 1008–1020 cm^{-1} (Fig. 9b). These were attributed to Si–O stretching adsorption, which can be observed in various silicates (Farmer, 1958; Petit et al., 2015). The positions of the Si–O bands are known to shift toward 950 cm^{-1} as the amount of Fe^{3+} in the tetrahedral sheets increases (Baron et al., 2016). Thus, the positions at 1008–1020 cm^{-1} suggest that the F-M-S-H and nontronite-like mineral had little or no tetrahedral Fe^{3+} (Baron et al., 2016; Petit et al., 2015).

The FTIR spectra of all samples contained bands in the range between 440 and 447 cm^{-1} (Fig. 9b). These

https://doi.org/10.1007/s42860-022-00197-2 Published online by Cambridge University Press

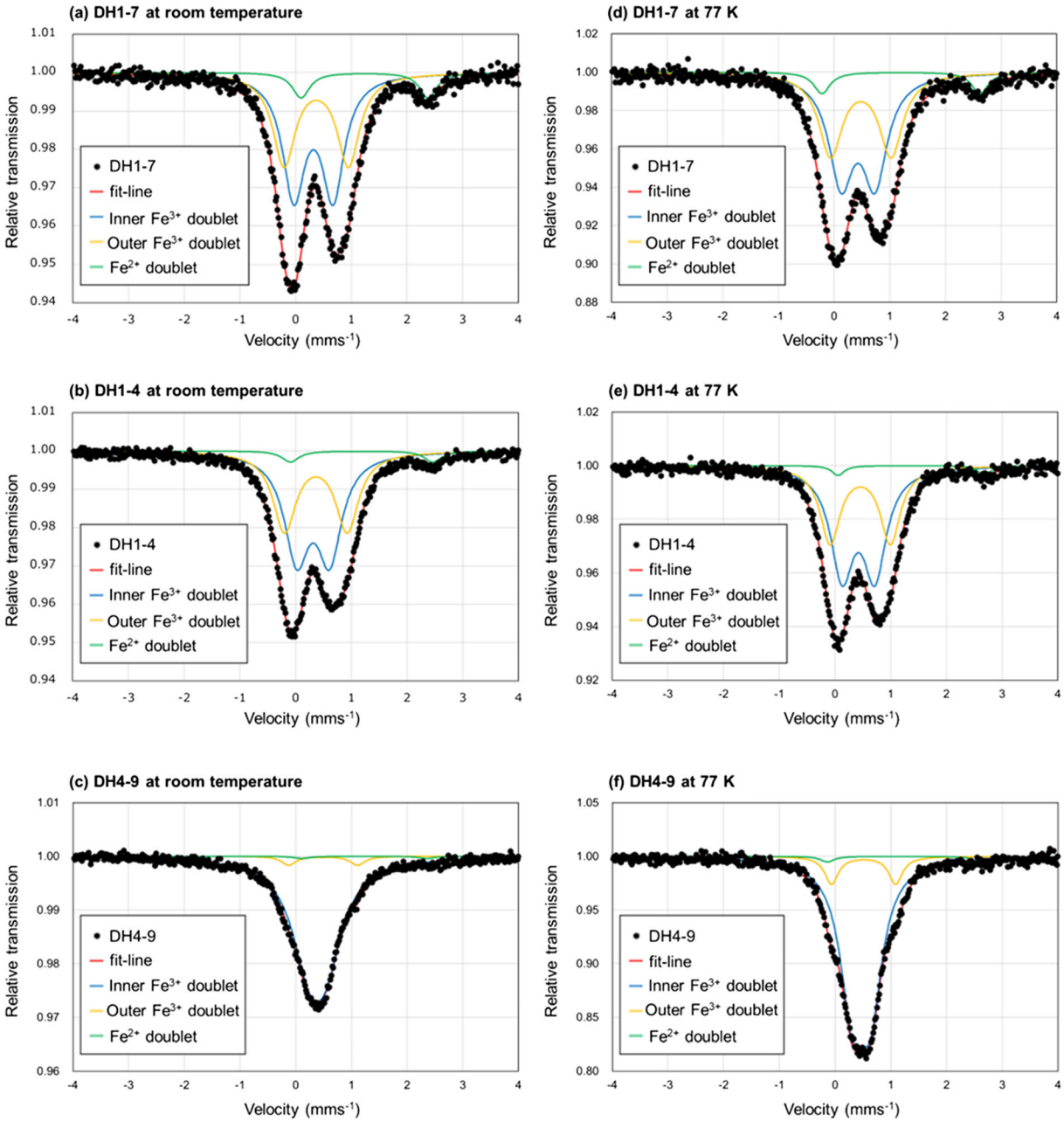

Fig. 8. Representative Mössbauer spectra: **a** DH1-7 measured at room temperature; **b** DH1-4 measured at room temperature; **c** DH4-9 measured at room temperature; **d** DH1-7 measured at 77 K; **e** DH1-4 measured at 77 K; **f** DH4-9 measured at 77 K

bands occurred in similar positions to in-plane Mg–O vibrations from serpentine (Yariv & Heller-Kallai, 1975), and were also recognized in the IR spectra of saponite (Madejová et al., 2011). The band around 670 cm^{-1} appeared in the F-M-S-H samples at DH1-7, and the associated band shoulders were recognized in the F-M-S-H sample at DH1-4 and in the nontronite-like mineral at DH4-9 (Fig. 9b). They were also recognized in several Mg-rich smectites (Benhammou et al., 2009; Grauby et al., 1994; Shimoda, 1971), and attributed to Mg_3–OH vibrations (Grauby et al., 1994).

Small bands in the range 613–616 cm^{-1} were observed in all samples (Fig. 9b), but were difficult to assign; the bands occurred in similar positions to Si–O–Al bonds of

https://doi.org/10.1007/s42860-022-00197-2 Published online by Cambridge University Press

Table 3 Computed Mössbauer parameters measured at room temperature

		IS (mm s^{-1})	QS (mm s^{-1})	FWHM (mms^{-1})	Area ratio (%)
DH1-7	Inner Fe^{3+} doublet	+ 0.32	0.71	0.48	52
	Outer Fe^{3+} doublet	+ 0.37	1.15	0.49	40
	Fe^{2+} doublet	+ 1.24	2.28	0.37	8
DH1-4	Inner Fe^{3+} doublet	+ 0.32	0.59	0.54	56
	Outer Fe^{3+} doublet	+ 0.36	1.12	0.50	40
	Fe^{2+} doublet	+ 1.18	2.55	0.37	4
DH4-9	Inner Fe^{3+} doublet	+ 0.38	0.30	0.75	95
	Outer Fe^{3+} doublet	+ 0.49	1.23	0.31	4
	Fe^{2+} doublet	+ 1.23	2.24	0.36	1

tetrahedral Si–O and octahedral Al–O, however, which were observed for synthetic dioctahedral smectite (Petit et al., 2015). Thus, the small bands are probably derived from small amounts of Al in the octahedral sheets of F-M-S-H and the nontronite-like mineral. A small band at 857 cm^{-1} appeared only in the F-M-S-H samples at DH1-4 (Fig. 9b), but the attribution of the band is still debated (Petit et al., 2015).

The FTIR spectra of the nontronite-like mineral exhibited bands at 820 cm^{-1}, while those of F-M-S-H showed only small bands at 816–820 cm^{-1} (Fig. 9b). These bands were related to Fe_2^{3+}–OH vibrations from nontronite (Baron et al., 2016; Decarreau et al., 2008; Grauby et al., 1994). Unlike F-M-S-H , the nontronite-like minerals exhibited bands at 764 and 493 cm^{-1} (Figure 9b). The band at 764 cm^{-1} was attributed to Fe^{3+}–Mg–OH vibrations, which were also observed in Fe^{3+}-rich montmorillonite (Petit et al., 2002). The band at 493 cm^{-1} was assigned to the change in Si–O–Fe^{3+} vibrations, which were also recognized in nontronite (Baron et al., 2016).

XRD Analysis and Chemical Composition after Acid or Alkylammonium Treatment of DH1-7

The expansion properties induced through the EG treatment of F-M-S-H (DH1-7) were unchanged regardless of the acid treatment (Figs 4a and 10). Nevertheless, peak shifts occurred in acid-treated F-M-S-H after heating. Specifically, without acid treatment practically no change in its peak positions was observed after heating at 250°C (Fig. 2a; Shimbashi et al., 2020), but after acid treatment a small peak at ~10 Å was observed (Fig. 10). The chemical compositions of the acid-treated F-M-S-H in DH1-7 were primarily composed of Fe, Mg, Si, and Al ions. The (Fe+Mg)/(Si+Al) ratio and the (Fe+Mg+Al)/Si ratio decreased, while the Fe/Mg ratio did not change significantly after the acid treatment

Table 4 Computed Mössbauer parameters measured at 77 K

		IS (mms^{-1})	QS (mms^{-1})	FWHM (mms^{-1})	Area ratio (%)
DH1-7	Inner Fe^{3+} doublet	+ 0.43	0.61	0.53	53
	Outer Fe^{3+} doublet	+ 0.48	1.09	0.51	40
	Fe^{2+} doublet	+ 1.20	2.84	0.36	7
DH1-4	Inner Fe^{3+} doublet	+ 0.42	0.59	0.50	59
	Outer Fe^{3+} doublet	+ 0.45	1.09	0.44	38
	Fe^{2+} doublet	+ 1.37	2.63	0.26	3
DH4-9	Inner Fe^{3+} doublet	+ 0.47	0.33	0.52	87
	Outer Fe^{3+} doublet	+ 0.51	1.15	0.30	11
	Fe^{2+} doublet	+ 1.22	2.73	0.30	2

https://doi.org/10.1007/s42860-022-00197-2 Published online by Cambridge University Press

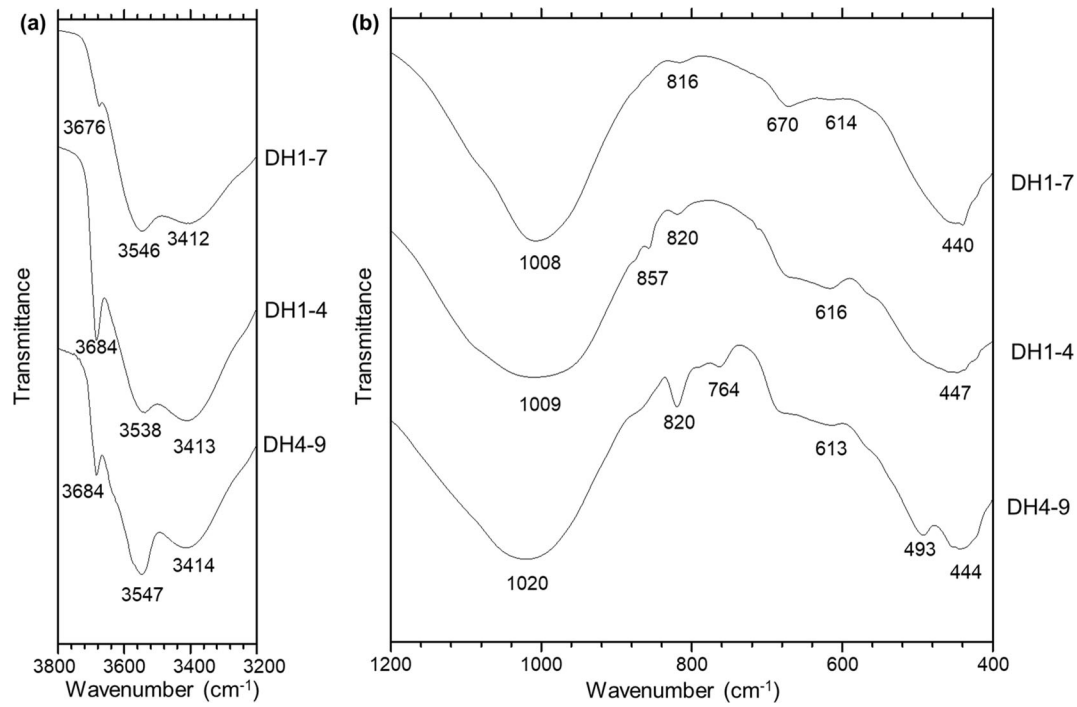

Fig. 9. Representative FTIR spectra of DH1-7, DH1-4, and DH4-9

(Fig. 11a, b, and c). Moreover, Ca ions were not detected after acid treatment (Fig. 11d).

When the alkylammonium treatment was conducted for the F-M-S-H in DH1-7, the 001 peak of F-M-S-H shifted from 14.6 to 21.1 Å (Fig. 12). The (Fe+Mg)/(Si+Al) ratio, the (Fe+Mg+Al)/Si ratio, and the Fe/Mg ratio of the F-M-S-H in DH1-7 did not change significantly after the alkylammonium treatment (Fig. 11a, b, and c). In addition, Ca ions were not detected after alkylammonium treatment (Fig. 11d).

Discussion

F-M-S-H

Imperfect interlayer hydroxide sheets

F-M-S-H displayed an XRD peak at 14 Å (Fig. 4a and c). However, the expandability after EG treatment and the dehydration behavior of F-M-S-H showed distinct differences from chlorite and smectite (Shimbashi et al., 2020). The unusual peak shift due to EG treatments and heating was similar to that of previously reported swelling chlorite and hydroxy-interlayered smectites (HIS). Swelling chlorite and HIS exhibited less expandability during EG treatment than smectite (swelling chlorite: Shimoda, 1974; HIS: Meunier, 2007), although in certain instances, swelling chlorite showed a similar expandability to smectite (Bain & Russell, 1981; Stephen & MacEwan, 1950). In addition, swelling chlorite and HIS also exhibited a different dehydration peak shift compared to smectite (Bain & Russell, 1981; Meunier, 2007; Stephen & MacEwan, 1950). Bain and Russell (1981) showed that this XRD behavior of swelling chlorite is due to the interlayer hydroxide sheet being imperfect and present in small amounts i.e. enough to allow organic molecules in the interlayer to expand the structure, but enough to prevent structural shrinkage after heating. Therefore, the similarities between F-M-S-H and swelling chlorite or HIS imply that F-M-S-H contains imperfect interlayer hydroxide sheets between TOT layers.

According to the IR and the Mössbauer spectra, the (Fe+Mg)/(Si+Al) or (Fe+Mg+Al)/Si ratio indicates the ratio of octahedral to tetrahedral cations in the F-M-S-H, although the coordination of Al ions remains uncertain owing to its small amount. The decrease in the (Fe+Mg)/(Si+Al) and (Fe+Mg+Al)/Si ratios of F-M-S-H at DH1-7 caused by the acid treatment (Fig. 11a and b) implied that the number of octahedral cations decreased in comparison to those in tetrahedral coordination. In addition, as the

https://doi.org/10.1007/s42860-022-00197-2 Published online by Cambridge University Press

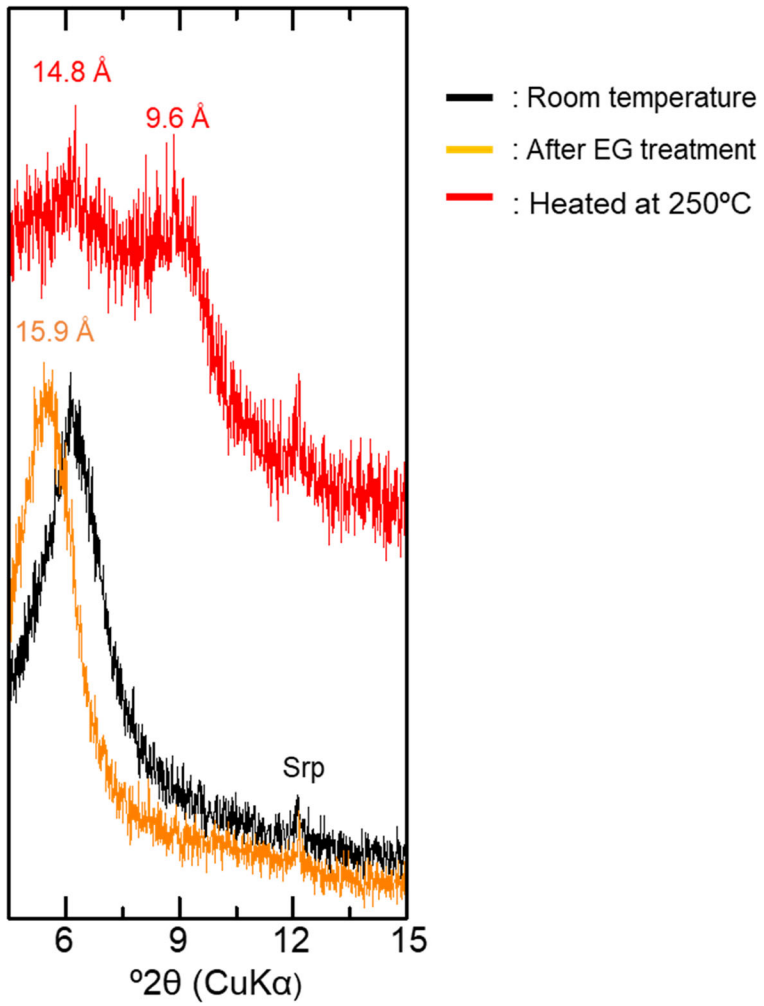

Fig. 10. XRD profile of acid-treated DH1-7 and that after EG treatment or heating at 250°C; Srp: serpentine

peak at 10 Å appeared on the XRD profile during the heating of acid-treated F-M-S-H (Fig. 10), the acid treatment dissolved preferentially the imperfect interlayer hydroxide sheets, subsequently causing structural shrinkage of the TOT layers during heating. Indeed, a previous study reported that hydroxide sheets between the TOT layers were partially dissolved when swelling chlorite was immersed in acid (Rich & Bonnet, 1975). In summary, supported by the results of characterization after acid treatment, F-M-S-H has Fe- and Mg-bearing imperfect interlayer hydroxide sheets between TOT layers.

Adsorbed cations and charges

The peak shift of F-M-S-H at DH1-7 induced by alkylammonium treatment indicated that F-M-S-H expanded due to the intercalation of alkylammonium ions (Fig. 12). As the only change observed in the chemical compositions after alkylammonium treatment was a decrease in Ca ions (Fig. 11), the Ca ions were probably adsorbed initially into the F-M-S-H interlayer and exchanged with alkylammonium ions during the treatment.

Although alkylammonium treatments have been used commonly to measure the layer charge of smectites and vermiculites (Lagaly & Weiss, 1969; Olis et al., 1990), the presence of interlayer hydroxide sheets in F-M-S-H prevented the determination of layer charge. Thus, the maximum layer charge derived from isomorphous substitution, which was obtained by assuming that all Al ions were tetrahedral, was calculated from the median value of the Al/(Si+Al) ratios (Table 2). The maximum negative charge due to the isomorphous substitution of F-M-S-H at DH1-7 was 0.44 per $O_{10}(OH)_2$ in TOT layers. On the other hand, the positive charge

https://doi.org/10.1007/s42860-022-00197-2 Published online by Cambridge University Press

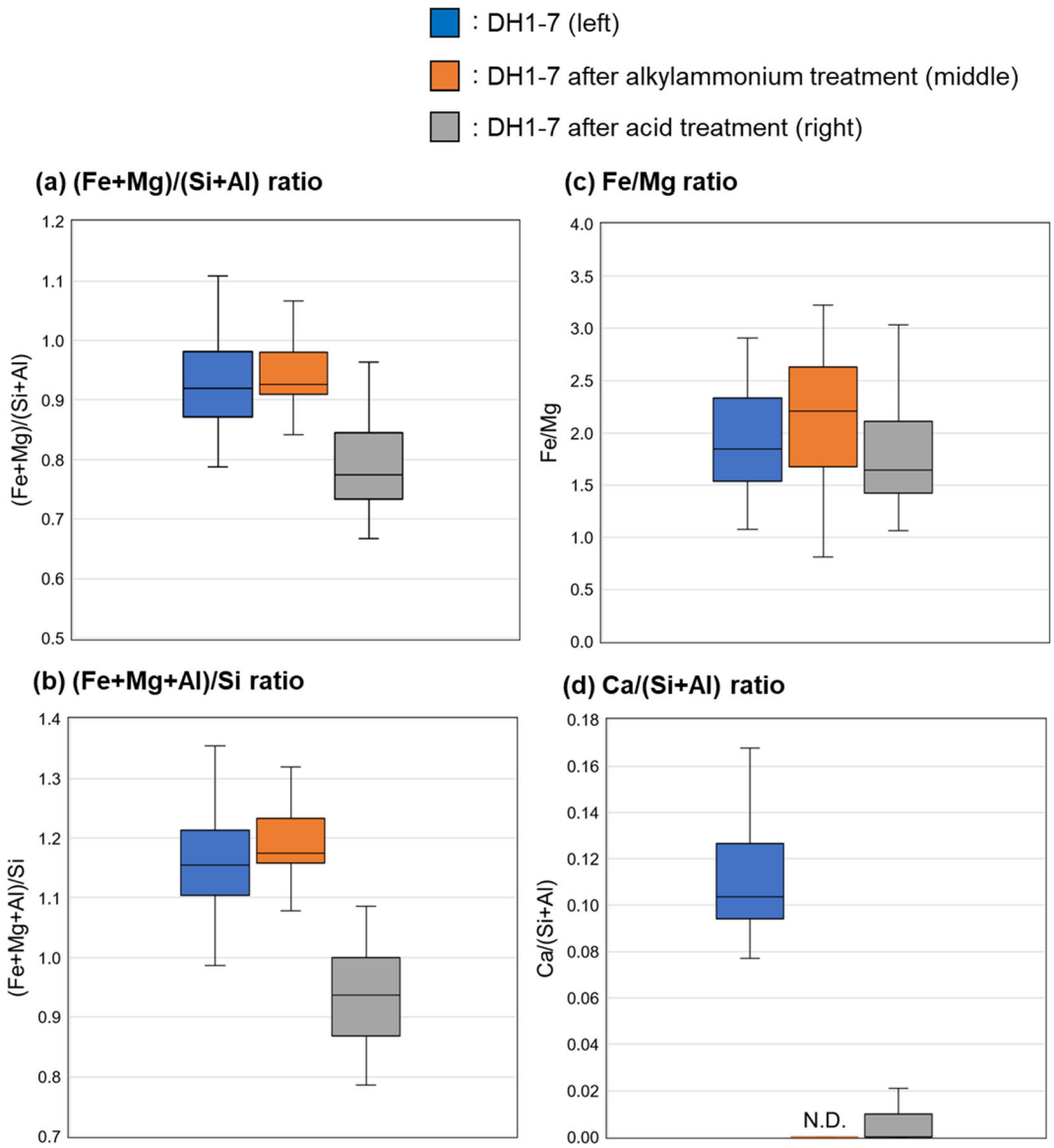

Fig. 11. Chemical composition of the samples before and after acid treatments or alkylammonium treatment; results are expressed as box-and-whisker plots. The solid line in the middle of the box represents the median values, whereas the ends of the boxes display the locations of the first and third quartiles (Q1 and Q3). The ends of the whiskers extend to the lowest and highest observations inside the region defined by Q1 – 1.5 (Q3–Q1) and Q3 + 1.5 (Q3–Q1). Values that fall beyond the whiskers are not plotted

due to adsorbed Ca ions at DH1-7 was 0.83 per $O_{10}(OH)_2$ in TOT layers, which was calculated from the Ca/(Si+Al) ratios (Table 2). The charge imbalances could be derived from the defect of cations in octahedral sheets and from anomalously high variable charges. If assuming the charge imbalances can be explained by only the additional considerations surrounding the defect of divalent cations in octahedral sheets, such as stevensite, the number of cations in octahedral sheets could be 2.81 per $O_{10}(OH)_2$ in TOT layers. On the other hand, it seems more plausible to consider the anomalously high variable charges derived from smaller particle size or from less crystallinity than in optimum TOT layers, based on the fact that F-M-S-H exhibited relatively broader peaks and lower intensities on the XRD profile of the <2 μm fractions (Shimbashi et al., 2020; Fig. 4a and c). According to the median values of the Al/(Si+Al) ratios and the Ca/(Si+Al) ratios of other F-M-S-

https://doi.org/10.1007/s42860-022-00197-2 Published online by Cambridge University Press

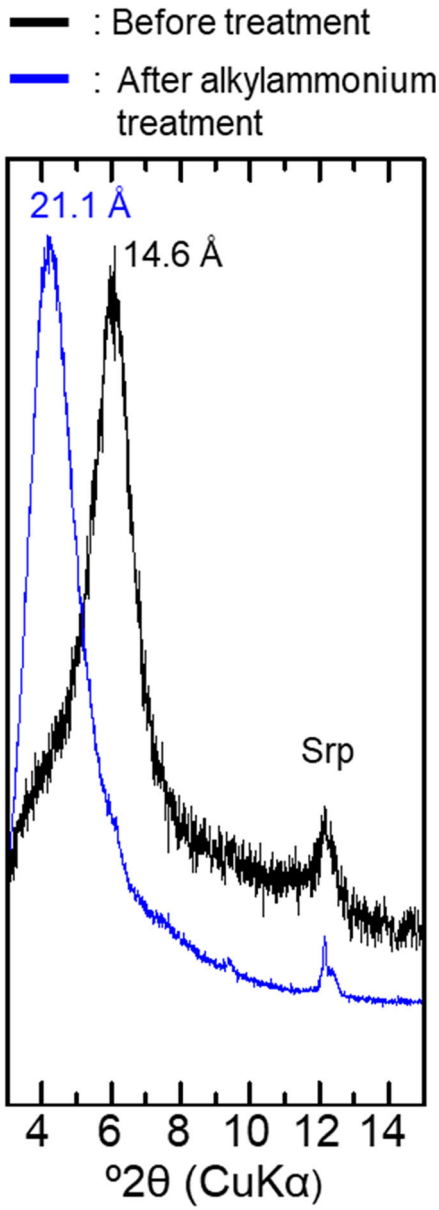

Fig. 12. XRD profile of DH1-7 before and after alkylammonium treatment of oriented samples; Srp: serpentine

H (Table 2), the negative charge derived from the defect of octahedral cations and from anomalously high variable charge should be considered for all F-M-S-H.

Unusual trioctahedral clay with Fe^{3+} as a major element

The major d_{060} values of F-M-S-H suggested a similarity to trioctahedral phyllosilicates (e.g. Fig. 4b and d). This is consistent with the fact that the FTIR results of F-M-S-H were indicative primarily of trioctahedral characteristics (Fig. 9b), although some dioctahedral characteristics were also present among the FTIR spectra. Nevertheless, the Mössbauer spectra showed that F-M-S-H is rich in ferric iron (Tables 3 and 4), suggesting a dioctahedral character based on the common Fe^{3+}-rich phyllosilicates. The F-M-S-H samples thus appear to have characteristics different from common phyllosilicates in that they have a trioctahedral character even though some Fe^{3+} is present.

Previous studies reported a rapid oxidation of ferrous iron-bearing smectite in glassy rhyolitic tuffs in Japan (Kohyama et al., 1973). Similarly, the oxidation of ferrous iron-bearing smectite was recognized in a gabbro saprolite in Canada (Kodama et al., 1988) as well as in basaltic rocks in the USA (Treiman et al., 2014). These clays displayed a d_{060} value similar to trioctahedral phyllosilicates although they contained certain amounts of Fe^{3+}. The FTIR spectra of these clays displayed bands in similar positions to those of Mg-rich trioctahedral phyllosilicates (Kodama et al., 1988; Kohyama et al., 1973). In addition, the Mössbauer spectra revealed high QS values (Treiman et al., 2014), which was also the case for the F-M-S-H. The increase in QS values may derive from the distortion of crystallographic sites (Dyar et al., 2006) or from low crystallinity (Baron et al., 2017). Because Kohyama et al. (1973) and Treiman et al. (2014) suggested previously that the lattice in oxidized ferrous iron-bearing smectite becomes distorted or contracted, the more plausible assumption here is that the high QS values exhibited were due mainly to distortion through oxidation. Thus, F-M-S-H exhibited similar characteristics to those of the oxidized ferrous iron-bearing smectite from various regions, indicating that F-M-S-H was initially ferrous and then was oxidized.

Variation with sampling depths and formation pathway

The decreases in the (Fe+Mg)/(Si+Al) and (Fe+Mg+Al)/Si ratios of F-M-S-H as sampling depths increased suggested that the number of octahedral cations decreased relative to those in tetrahedral coordination (Fig. 7a and b). In addition, the peaks observed at ~10 Å during heating, which were indicative of a domain without interlayer hydroxide sheets, appeared with increasing sampling depths (Fig. 2; Shimbashi et al., 2020). The implication is, therefore, that the number of interlayer hydroxide sheets of F-M-S-H decreased gradually with increasing sampling depth, and

https://doi.org/10.1007/s42860-022-00197-2 Published online by Cambridge University Press

formed smectitic domains (i.e. domains without interlayer hydroxide sheets; Fig. 13).

One possibility that led to a relative decrease in interlayer hydroxide sheets with sampling depth could be that changes occurred in the mineral assemblage of the remaining primary minerals. Shimbashi et al. (2020) suggested that Mg-rich olivine was present in the initial sediments and dissolved through an interaction with alkaline seepage. After olivine had dissolved, the primary minerals which remained (e.g. pyroxene, amphibole) exhibited smaller (Mg+Fe)/Si ratios. If this change in the mineral assemblage of primary minerals leads to the gradual alteration of F-M-S-H, one would expect that F-M-S-H will gradually alter to show smaller (Fe+Mg)/Si ratios, i.e. the relative decrease in interlayer hydroxide sheets.

A previous study at the focal site reported a positive linear correlation between sampling depths and the depositional ages of the sediments (Table 1; Shimbashi et al., 2020). If the sediments interacted with alkaline seepage after deposition, it is considered that the deeper sediments were interacting with alkaline seepage for a longer period. Therefore, although the cause of the change in the expandability, the Fe/Mg ratios, and the

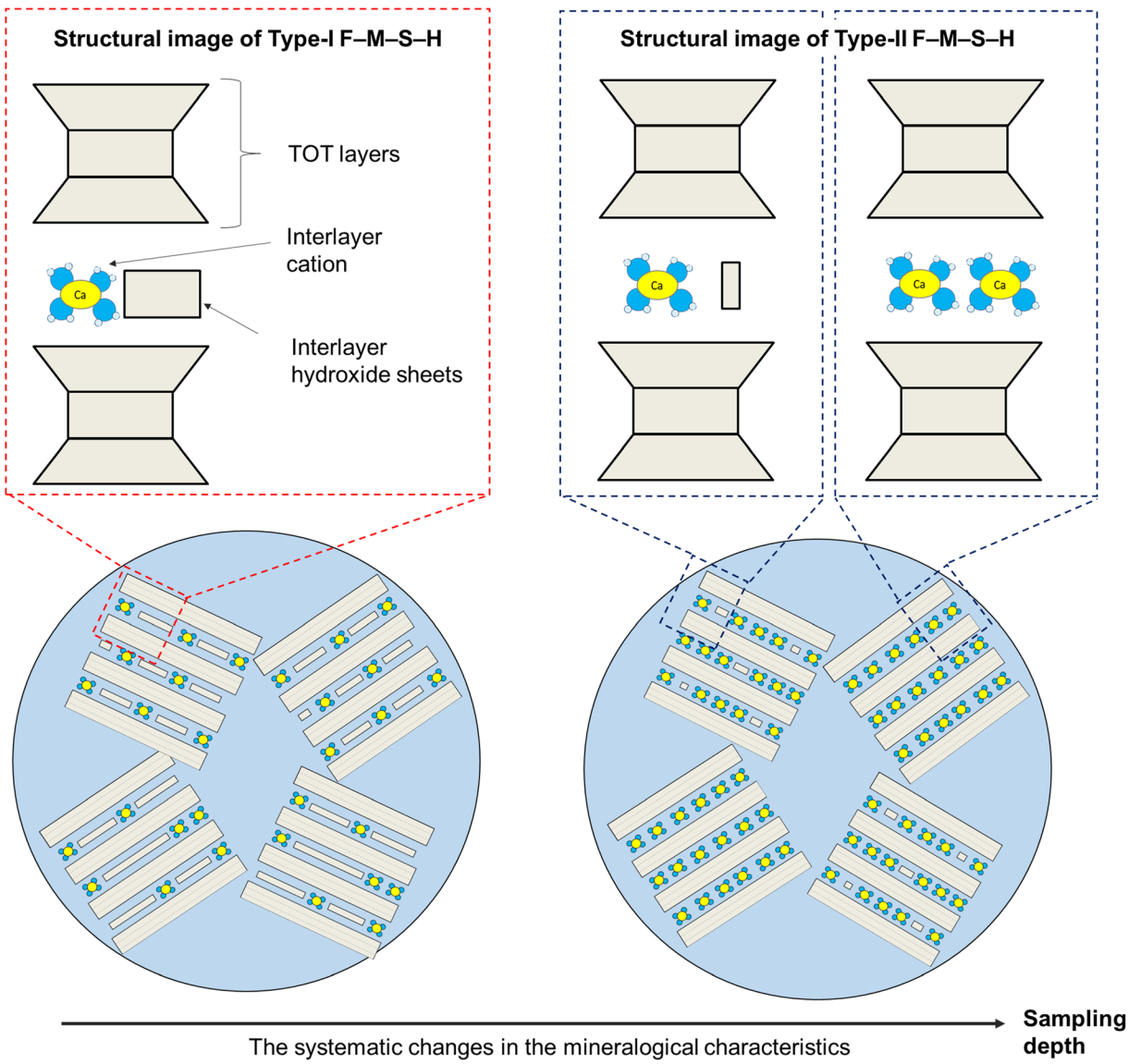

Fig. 13. Schematic of the F-M-S-H structural characteristics with different sampling depths

https://doi.org/10.1007/s42860-022-00197-2 Published online by Cambridge University Press

Al/(Si+Al) ratios of F-M-S-H remains uncertain (Figs 5 and 7), the mineralogical changes exhibited in association with increasing sampling depths were also probably caused by the varied interaction periods between each sediment at different sampling depths and alkaline seepage. In addition, worth noting is that changes in the characteristics of F-M-S-H according to sampling depth should have already been observed prior to the oxidation event. This is because changes in the characteristics of F-M-S-H in its ferrous form (F^{2+}–M–S–H) at deeper depths should have already been initiated due to its interaction between the sediments and alkaline seepage, concurrently with the formation of F^{2+}–M–S–H at shallower depths under relatively reducing conditions. Thus, F-M-S-H might have been oxidized, for example, after sample collection.

Nontronite-like Mineral

Structural and chemical characteristics

The nontronite-like mineral displayed an XRD peak at 14 Å and exhibited the same expandability after EG treatment as ideal smectite (d_{001} at 17 Å) (Fig. 4e and Table 1). The results of the major d_{060} on the XRD analysis were suggestive of Fe^{3+}-rich dioctahedral sheets (i.e. nontronite) (Fig. 4f). The predominant inner-doublet of the nontronite-like mineral in the Mössbauer spectra suggested that Fe^{3+} ions were present in octahedral coordination in an environment similar to that of Fe^{3+} at the octahedral site of the ideal nontronite. Moreover, the chemical composition of the nontronite-like mineral showed that both Fe and Mg were predominant (Fig. 6a). Although Mg_3–OH vibrations in the FTIR spectra could be derived partly from traces of serpentine in the <2 μm fraction (Fig. 4e), these bands were also observed in Fe^{3+}- and Mg-bearing smectites (Grauby et al., 1994). Thus, all of the data above indicated that the 14 Å phase in DH4-9 can be assigned to nontronite containing certain amounts of Mg in the octahedral sheets.

In contrast, the peak that indicated no structural shrinkage upon heating at 250°C suggested the presence of a phase different from ideal nontronite (Fig. 3; Shimbashi et al., 2020). Considering the same for F-M-S-H, this indicated that an imperfect interlayer hydroxide sheet was present partly between layers of nontronite – the 14 Å phase; this is referred to as the nontronite-like mineral, consisting of nontronite, partly including the interlayer hydroxide sheet.

Formation Pathway

Distinct differences in chemical compositions and Fe sites between the F-M-S-H and the nontronite-like mineral were recognized (Figs 6b and 8). Shimbashi et al. (2020) suggested that the F-M-S-H was formed as the result of the interaction between sediments and alkaline seepage without the involvement of seawater, whereas the nontronite-like mineral formed from the interaction with seawater infiltration. Therefore, the distinct differences between F-M-S-H and the nontronite-like mineral can be attributed to these phases being formed under different chemical conditions.

Considering that nontronite can form under various redox conditions from either Fe^{2+} or Fe^{3+} starting gels (Petit et al., 2017), several pathways for nontronite formation are possible. For example, Decarreau and Bonnin (1986) and Decarreau et al. (2008) reported that nontronite formed through an initial Fe^{2+}-bearing precipitate and subsequent oxidation (Pathway I). In addition, Decarreau et al. (1987) reported that the synthesis of smectite at low temperatures from solutions that contained Fe^{3+} ions without Fe^{2+} or Mg ions was also possible (Pathway II), although the crystal growth of a ferric smectite under those conditions was slow. Gainey et al. (2017) reported that dioctahedral Fe-rich clay minerals, such as nontronite, can be formed rapidly from aqueous Fe^{3+} in the presence of at least small amounts of aqueous Mg (Pathway III).

Regarding the formation of the nontronite-like mineral at the study site, the likelihood that it formed through the Pathway II process was low; this is because a certain amount of Mg was recognized in its chemical composition (Fig. 6a). Moreover, if the nontronite-like mineral was formed through Pathway I, an ejection of ferric iron from the octahedral sheets with oxidation and the formation of iron oxides either inside or outside the interlayer would be expected to occur to form a dioctahedral sheet of nontronite-like mineral. However, the formation of interlayer hydroxide sheets by the ejected ferric iron was not plausible in the present study because the chemical composition of the nontronite-like mineral exhibited a similarity to nontronite (Fig. 6b). Moreover, the formation of iron oxides outside the nontronite-like mineral were not observed during the current analysis, so formation through Pathway I was

https://doi.org/10.1007/s42860-022-00197-2 Published online by Cambridge University Press

not likely. From the above consideration, the nontronite-like mineral possibly was precipitated directly in the presence of aqueous Fe^{3+} and Mg ions (i.e. Pathway III).

In contrast to F-M-S-H, the nontronite-like mineral exhibited no significant changes in expandability and chemical composition with varying sampling depths (Figs 5 and 7). This indicates no correlation between the structural and chemical characteristics of the nontronite-like mineral and the period of interaction between the sediments and alkaline seepage. The depositional environment of the sediments probably changed from seawater to brackish and then to freshwater, and the nontronite-like mineral was thought to be formed during a period of seawater infiltration (Shimbashi et al., 2020). This indicates that the nontronite-like mineral has likely been stable under present-day alkaline conditions for thousands of years (Table 1), after the cessation of seawater infiltration.

Conclusions

In order to predict the potential alteration of the constituent minerals in radioactive-waste disposal facilities, understanding secondary mineral species under natural alkaline conditions is important. A previous study reported uncommon Fe- and Mg-bearing clays, referred to as F-M-S-H and nontronite-like minerals, which were formed under natural alkaline conditions (Shimbashi et al., 2020). In the current study, the structural and chemical characteristics and formation pathways of these clays were investigated.

F-M-S-H comprised TOT layers, imperfect interlayer hydroxide sheets, and interlayer Ca ions. F-M-S-H was previously of a ferrous form, and systematic changes, such as the gradual decrease of the interlayer hydroxide sheets to create smectitic domains, occurred during the interaction between each sediment at different sampling depths and alkaline seepage. Furthermore, F-M-S-H likely oxidized after sample collection.

The nontronite-like mineral comprised nontronite and partly included an interlayer hydroxide sheet. The nontronite-like mineral was formed under different chemical conditions from F-M-S-H, likely having been precipitated in the presence of aqueous Fe^{3+} and Mg ions during a period of seawater infiltration. Mineralogical changes did not occur after the cessation of seawater infiltration, at least among the timescales observed at the study site, i.e. they were likely stable under present-alkaline conditions for thousands of years.

Acknowledgments This study was carried out as part of the Natural Analogue project within the "Advanced technology development for geological disposal of TRU waste" program commissioned by the Agency for Natural Resources and Energy in the Ministry of Economy, Trade and Industry of Japan. The authors thank Dr Fujii Naoki from Radioactive Waste Management Funding and Research Center for the principal management of the project. They also thank Dr Minoru Yamakawa from the Radioactive Waste Management Funding and Research Center, Mr Masanobu Nishimura and Mr Yukinobu Kimura of the Obayashi Corporation, Dr W. Russell Alexander from Bedrock Geosciences, and Professor Carlo Arcilla at the University of the Philippines for the field survey. Dr Yasutaka Watanabe and Dr Daisuke Minato from the Central Research Institute of Electric Power Industry are acknowledged for their help and valuable comments for performing research at this site. The authors thank the two anonymous reviewers for considerably improving the manuscript.

Funding This work was funded by JSPS KAKENHI (grant number JP19H00878).

Data availability The datasets generated during and/or analyzed during the current study are available from the corresponding author on reasonable request.

Code availability Not applicable

Declarations

Conflicts of interest The authors declare that they have no conflict of interest.

References

Akbulut, A., & Kadir, S. (2003). The geology and origin of sepiolite, palygorskite and saponite in Neogene lacustrine sediments of the Serinhisar-Acipayam basin, Deńizli, SW Turkey. *Clays and Clay Minerals, 51*, 279–292.

Aurelio, M. A., Forbes, M. T., Taguibao, K. J. L., Savella, R. B., Bacud, J. A., Franke, D., Pubellier, M., Savva, D., Meresse, F., Steuer, S., & Carranza, C. D. (2014). Middle to Late Cenozoic tectonic events in south and central Palawan (Philippines) and their implications to the evolution of the south-eastern margin of South China Sea: Evidence from onshore structural and offshore seismic data. *Marine and Petroleum Geology, 58*, 658–673.

Bain, D. C., & Russell, J. D. (1981). Swelling minerals in a basalt and its weathering products from Morvern, Scotland: II. Swelling chlorite. *Clay Minerals, 16*, 203–212.

https://doi.org/10.1007/s42860-022-00197-2 Published online by Cambridge University Press

Barnes, I., O'Neil, J. R., & Trescases, J. J. (1978). Present day serpentinization in New Caledonia, Oman and Yugoslavia. *Geochimica et Cosmochimica Acta, 42*(1), 144–145.

Baron, F., Petit, S., Pentrák, M., Decarreau, A., & Stucki, J. W. (2017). Revisiting the nontronite Mössbauer spectra. *American Mineralogist, 102*(7), 1501–1515.

Baron, F., Petit, S., Tertre, E., & Decarreau, A. (2016). Influence of aqueous Si and Fe speciation on tetrahedral Fe (III) substitutions in nontronites: A clay synthesis approach. *Clays and Clay Minerals, 64*(3), 230–244.

Benhammou, A., Tanouti, B., Nibou, L., Yaacoubi, A., & Bonnet, J. P. (2009). Mineralogical and physicochemical investigation of Mg-smectite from Kbel Ghassoul, Morocco. *Clays and Clay Minerals, 57*, 264–270.

Brindley, G. W., Bish, D. L., & Wan, H. M. (1979). Compositions, structures, and properties of nickel-containing minerals in the kerolite-pimelite series. *American Mineralogist, 64*, 615–625.

Craw, D., Landis, C. A., & Kelsey, P. I. (1987). Authigenic chrysotile formation in the matrix of Quaternary debris flows, northern Southland, New Zealand. *Clays and Clay Minerals, 35*, 43–52.

Czaja, M., Kadziołka-Gaweł, M., Lisiecki, R., Bodył-Gajowska, S., & Mazurak, Z. (2014). Luminescence and other spectroscopic properties of purple and green Cr-clinochlore. *Physics and Chemistry of Minerals, 41*, 115–126.

Dauzeres, A., Achiedo, G., Nied, D., Bernard, E., Alahrache, S., & Lothenbach, B. (2016). Magnesium perturbation in low-pH concretes placed in clayey environment—solid characterizations and modeling. *Cement and Concrete Research, 79*, 137–150.

Decarreau, A., & Bonnin, D. (1986). Synthesis and crystallogenesis at low temperature of Fe (III)-smectites by evolution of coprecipitated gels: experiments in partially reducing conditions. *Clay Minerals, 21*(5), 861–877.

Decarreau, A., Bonnin, D., Badaut-Trauth, D., Couty, R., & Kaiser, P. (1987). Synthesis and crystallogenesis of ferric smectite by evolution of Si-Fe coprecipitates in oxidizing conditions. *Clay Minerals, 22*(2), 207–223.

Decarreau, A., Petit, S., Martin, F., Farges, F., Vieillard, P., & Joussein, E. (2008). Hydrothermal synthesis, between 75 and 150°C, of high-charge, ferric nontronites. *Clays and Clay Minerals, 56*(3), 322–337.

Dyar, M. D., Agresti, D. G., Schaefer, M. W., Grant, C. A., & Sklute, E. C. (2006). Mössbauer spectroscopy of earth and planetary materials. *Annual Reviews of Earth and Planetary Science, 34*, 83–125.

Farmer, V. C. (1958). The infra-red spectra of talc, saponite, and hectorite. *Mineralogical Magazine, 31*, 829–845.

Fernández, R., González-Santamaría, D., Angulo, M., Torres, E., Ruiz, A. I., Turrero, M. J., & Cuevas, J. (2018). Geochemical conditions for the formation of Mg silicates phases in bentonite and implications for radioactive waste disposal. *Applied Geochemistry, 93*, 1–9.

Fujii, N., Yamakawa, M., Shikazono, N., & Sato, T. (2014). *Geochemical and Mineralogical Characterizations of Bentonite interacted with Alkaline Fluids generating in Zambales Ophiolite, Northwestern Luzons, Philippines*. *The Geological Society of Japan, 120*, 361–375 (in Japanese with English abstract).

Furquim, S. A. C., Barbiéro, L., Graham, R. C., de Queiroz Neto, J. P., Ferreira, R. P. D., & Furian, S. (2010). Neoformation of micas in soils surrounding an alkaline-saline lake of Pantanal wetland, Brazil. *Geoderma, 158*, 331–342.

Gainey, S. R., Hausrath, E. M., Adcock, C. T., Tschauner, O., Hurowitz, J. A., Ehlmann, B. L., Xiao, Y., & Bartlett, C. L. (2017). Clay mineral formation under oxidized conditions and implications for paleoenvironments and organic preservation on Mars. *Nature communications, 8*(1), 1–7.

García Calvo, J. L., Hidalgo, A., Alonso, C., & Fernández Luco, L. (2010). Development of low-pH cementitious materials for HLRW repositories. Resistance against ground waters aggression. *Cement and Concrete Research, 40*, 1290–1297.

Grauby, O., Petit, S., Decarreau, A., & Baronnet, A. (1994). The nontronite-saponite series: an experimental approach. *European Journal of Mineralogy, 6*, 99–112.

Johnston, J. H., & Cardile, C. M. (1985). Iron sites in nontronite and the effect of interlayer cations from Mössbauer spectra. *Clays and Clay Minerals, 33*, 21–30.

Kaufhold, S., Dohrmann, R., & Weber, C. (2020). Evolution of the pH value at the vicinity of the iron-bentonite interface. *Applied Clay Science, 201*, 105929.

Kodama, H., De Kimpe, C. R., & Dejou, J. (1988). Ferrian saponite in a gabbro saprolite at Mont Megantic, Quebec. *Clays and Clay Minerals, 36*, 102–110.

Kodama, H., Longworth, G., & Townsend, M. G. (1982). A Mössbauer investigation of some chlorites and their oxidation products. *The Canadian Mineralogist, 20*, 585–592.

Kohyama, N., Shimoda, S., & Sudo, T. (1973). Iron-rich saponite (ferrous and ferric forms). *Clays and Clay Minerals, 21*, 229–237.

Lagaly, G., & Weiss, A. (1969). *Determination of the layer charge in mica-type layer silicates. Pp. 61–80 in: Proceedings of the International Clay Conference, Tokyo, 1969, Volume 1 (L. Heller, editor)*. Israel University Press.

Lerouge, C., Gaboreau, S., Grangeon, S., Claret, F., Warmont, F., Jenni, A., … Mäder, U. (2017). In situ interactions between Opalinus clay and low alkali concrete. *Physics and Chemistry of the Earth, Parts A/B/C, 99*, 3–21.

Madejová, J. (2003). FTIR techniques in clay mineral studies. *Vibrational Spectroscopy, 31*, 1–10.

Madejová, J., Balan, E., & Petit, S. (2011). Application of vibrational spectroscopy to the characterization of phyllosilicates and other industrial minerals. *EMU Notes in Mineralogy, 9*, 171–226.

Meunier, A. (2007). Soil hydroxy-interlayered minerals: a reinterpretation of their crystallochemical properties. *Clays and Clay Minerals, 55*(4), 380–388.

Milodowski, A. E., Norris, S., & Alexander, W. R. (2016). Minimal alteration of montmorillonite following long-term interaction with natural alkaline groundwater: Implications for geological disposal of radioactive waste. *Applied Geochemistry, 66*, 184–197.

Nishiki, Y., Sato, T., Katoh, T., Otake, T., & Kikuchi, R. (2020). Precipitation of magnesium silicate hydrates in natural alkaline surface environments. *Clay Science, 24*, 1–13.

Olis, A. C., Malla, P. B., & Douglas, L. A. (1990). The rapid estimation of the layer charges of 2:1 expanding clays from a single alkylammonium ion expansion. *Clay Minerals, 25*, 39–50.

Petit, S., Baron, F., & Decarreau, A. (2017). Synthesis of nontronite and other Fe-rich smectites: a critical review. *Clay Minerals, 52*, 469–483.

Petit, S., Caillaud, J., Righi, D., Madejová, J., Elsass, F., & Köster, H. M. (2002). Characterization and crystal chemistry of an Fe-rich montmorillonite from Ölberg, Germany. *Clay Minerals, 37*(2), 283–297.

Petit, S., Decarreau, A., Gates, W., Andrieux, P., & Grauby, O. (2015). Hydrothermal synthesis of dioctahedral smectites: The Al-Fe^{3+} chemical series. Part II: Crystal-chemistry. *Applied Clay Science, 104*, 96–105.

Rich, C. I., & Bonnet, J. A. (1975). Swelling chlorite in a soil of the Dominican Republic. *Clays and Clay Minerals, 23*(2), 97–102.

RWMC. (2016). *Advancement of processing and disposal technique for the geological disposal of TRU waste (FY2015)*. https://www.enecho.meti.go.jp/category/electricity_and_gas/nuclear/rw/library/library06.html. Accessed 20 Apr 2022 (in Japanese).

RWMC. (2017). *Advancement of processing and disposal technique for the geological disposal of TRU waste (FY2016)*. https://www.enecho.meti.go.jp/category/electricity_and_gas/nuclear/rw/library/library06.html. Accessed 20 Apr 2022 (in Japanese).

RWMC. (2018). *Advancement of processing and disposal technique for the geological disposal of TRU waste (FY2017)*. https://www.enecho.meti.go.jp/category/electricity_and_gas/nuclear/rw/library/library06.html. Accessed 20 Apr 2022 (in Japanese).

Sellin, P., & Leupin, O. X. (2014). The use of clay as an engineered barrier in radioactive-waste management – a review. *Clays and Clay Minerals, 61*, 447–498.

Shimbashi, M., Sato, T., Yamakawa, M., Fujii, N., & Otake, T. (2018). Formation of Fe-and Mg-rich smectite under hyperalkaline conditions at Narra in Palawan, the Philippines. *Minerals, 8*(4), 155.

Shimbashi, M., Yokoyama, S., Watanabe, Y., Sato, T., Otake, T., Kikuchi, R., Yamakawa, M., & Fujii, N. (2020). Formation of natural silicate hydrates by the interaction of alkaline seepage and sediments derived from serpentinized ultramafic rocks at Narra, Palawan, the Philippines. *Minerals, 10*, 719.

Shimoda, S. (1971). Mineralogical studies of a species of stevensite from the Obori mine, Yamagata Prefecture, Japan. *Clay Minerals, 9*, 185–192.

Shimoda, S. (1974). 2,3 Properties of so-called swelling chlorite. *Journal of the Clay Science Society of Japan, 14*, 79–89 (in Japanese with English abstract).

Stephen, I., & MacEwan, D. M. C. (1950). Swelling chlorite. *Geotechnique, 2*, 82–83.

Treiman, A. H., Morris, R. V., Agresti, D. G., Graff, T. G., Achilles, C. N., Rampe, E. B., Bristow, T. F., Ming, D. W., Blake, D. F., Vaniman, D. T., Bish, D. L., Chipera, S. J., Morrison, S. M., & Downs, R. T. (2014). Ferrian saponite from the Santa Monica Mountains (California, U.S.A., Earth): Characterization as an analog for clay minerals on Mars with application to Yellowknife Bay in Gale Crater. *American Mineralogist, 99*, 2234–2250.

Wilson, J., Cressey, G., Cressey, B., Cuadros, J., Ragnarsdottir, K. V., Savage, D., & Shibata, M. (2006). The effect of iron on montmorillonite stability. (II) Experimental investigation. *Geochimica et Cosmochimica Acta, 70*(2), 323–336.

Yariv, S., & Heller-Kallai, L. (1975). The relationship between the IR spectra of serpentines and their structures. *Clays and Clay Minerals, 23*, 145–152.

Yokoyama, S., Shimbashi, M., Minato, D., Watanabe, Y., Jenni, A., & Mäder, U. (2021). Alteration of bentonite reacted with cementitious materials for 5 and 10 years in the Mont Terri Rock Laboratory (CI Experiment). *Minerals, 11*(3), 251.

Yoshida, H., Kitayama, K., Sato, T., & Kobayashi, Y. (2010). Natural analogues / Supporting geological disposal: Gaining evidence of predictability on 100 ka timescales. *The Atomic Energy Society of Japan: ATOMO , 52*(8), 473–477 (in Japanese).

Zazzi, Å., Hirsch, T. K., Leonova, E., Kaikkonen, A., Grins, J., Annersten, H., & Edén, M. (2006). Structural investigations of natural and synthetic chlorite minerals by x-ray diffraction, Mössbauer spectroscopy and solid-state nuclear magnetic resonance. *Clays and Clay Minerals, 54*, 252–265.

Zviagina, B. B., McCarty, D. K., Środoń, J., & Drits, V. A. (2004). Interpretation of infrared spectra of dioctahedral smectites in the region of OH-stretching vibrations. *Clays and Clay Minerals, 52*(4), 399–410.

https://doi.org/10.1007/s42860-022-00197-2 Published online by Cambridge University Press